Digitization, Measurement, and Analysis of a 1905 Barnard Atlas Photographic Plate

Rowen Glusman,[1] Lauren Boegen,[1] William Cerny,[1,2] Ali Chapman,[1] Isaiah Escapa,[1] Richard G. Kron,[1] Michael N. Martinez,[1] Amanda Muratore,[1] and Audrey P. Scott[1]

(Yerkes Photographic Plate Digitization Team)

[1]*Department of Astronomy and Astrophysics, University of Chicago,*
5640 S. Ellis Ave., Chicago IL 60637, USA
[2]*Kavli Institute for Cosmological Physics, University of Chicago,*
5640 S. Ellis Ave., Chicago, IL 60637, USA

ABSTRACT

In the second paper in this series, we improve on our previous demonstration of the ability of a commercially available graphic arts scanner and cost-effective analysis tools to produce scientifically useful scans of astronomical photographic plates. We describe a method using freely available tools to extract magnitude measurements from the star images on sky survey plates, such as are stored in observatory archives around the world. We detail the use of this method on one plate in particular, Plate 8 in E. E. Barnard's *Photographic Atlas of Selected Regions of the Milky Way* (1927); examine the effects of our scanning method on our magnitude measurements; discuss the difficulties encountered when measuring the magnitudes of stars in crowded fields; and present a case study of red supergiant stars appearing within the field. Our work results in a catalog of more than 66,000 measurements of stellar positions and magnitudes in the central 6.8×6.8 degree field of view.

Keywords: techniques: photometric; catalogs; surveys; atlases; astrometry; stars: variables: general; Milky Way; photographic plates

1. INTRODUCTION

Edward Emerson Barnard's *A Photographic Atlas of Selected Regions of the Milky Way* (hereafter *Atlas*) is one of many methodical sky surveys taken before 1950. These surveys far predate the CCDs that revolutionized modern astronomy. An astronomer at Yerkes Observatory from 1895 to 1923, Barnard specialized in the study of nebulous regions of the Milky Way. While observing at Mount Wilson Observatory in 1905, he documented the Milky Way as far south as his latitude would permit (the southernmost plate center in the series has a declination of -39.3 degrees) (Barnard et al. 1927). Mary Ross Calvert – computer, high-level assistant, and curator of the Yerkes photographic plate collection – prepared the *Atlas* charts under Barnard's supervision. Calvert also completed and refined his initial list of dark objects featured on the plates, performed the computations necessary for the completion of the *Atlas*'s many

tables, added annotations to the included plates, and shepherded the work to its eventual publication in 1927. In his preface to the *Atlas*, Yerkes Director Edwin B. Frost credits her with a "large share in the editorial duties." A digital version of the The original *Atlas* is accessible from the Georgia Institute of Technology.[1]

The photographs included in the *Atlas* were produced using second negatives created from the original plates. Many of these second negatives remain in the Yerkes Observatory plate vault in Williams Bay, Wisconsin; the original plates are at the University of Chicago. Barnard took these images with the 10-inch Bruce Telescope, which was specially fabricated for the purpose of making wide-field survey plates of the Milky Way. The telescope produced a series of 12-inch (13 degrees) square plates, most of which were taken at the Mount Wilson Observatory; the remainder at Yerkes Observatory. All were prepared with a blue-sensitive emulsion called "Seed 23." Of the Bruce Telescope's plates from this period, 50 were reproduced in the *Atlas*.

Corresponding author: Rowen Glusman
rowenisobel@uchicago.edu

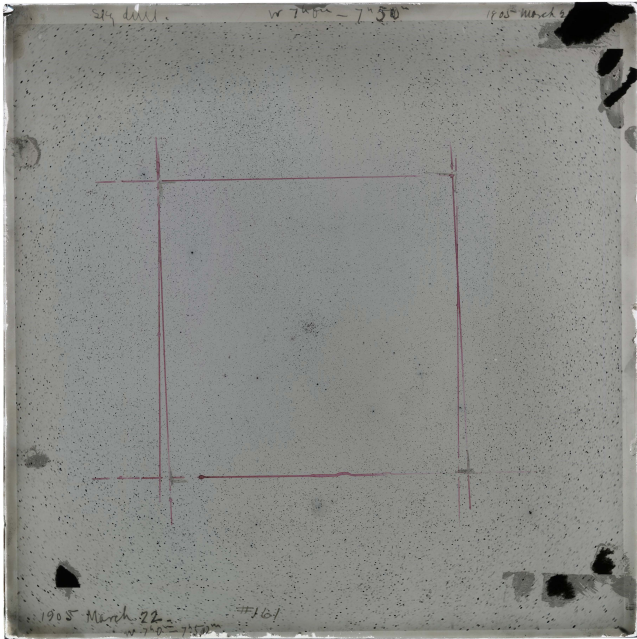[1] https://exhibit-archive.library.gatech.edu/barnard/

Figure 1. Plate 10B-161, taken on March 22, 1905 (local time), dimensions 12 x 12 inches. The field measures approximately 13° on a side, centered on the cluster M35. Other objects present on the plate include NGC 2158 and IC 444. The lines are original markings on the plate and indicate the area to be included in the *Atlas* as Plate 8.

Although astronomical research has advanced well past the age of photographic plates, these objects are still valuable. Working with photographic plates can be challenging: their data are analog; their materials physically fragile; and digitization results in "an observation of an observation" (Elizabeth Griffin, personal communication). However, the data on the plates extend the timescale over which astrophysical phenomena can be observed to over 100 years. Creating universal access to such irreproducible data is therefore a worthy goal, and one which many groups around the world are pursuing. Examples include the Wide-Field Plate Database (WFPDB; Tsvetkov et al. 2015), the Astronomical Photographic Data Archive (APDA; Castelaz 2009), and the Archives of Photographic PLates for Astronomical USE (APPLAUSE)[2]. Our goal in this work is to create a catalog of stellar magnitude measurements from a 1905 plate from Barnard's *Atlas* with low-cost, accessible tools and demonstrate its value for photometric variability studies.

An example of a program similar to ours is the scanning effort for the Sternberg Institute's astrograph (Kolesnikova et al. (2008), Sokolovsky et al. (2017)):

---

[2] https://www.plate-archive.org/applause/

similar plate scale, field-of-view, and magnitude limit. These authors also used a flatbed scanner and successfully applied their methods to measure light curves for variable stars on a large time series of plates. However it is accomplished, the process must take into account that photographic materials are non-linear detectors (see for example the detailed treatment in Moffat (1969)). The digitizer also introduces its own response, which can be non-trivial if it depends on local gradients such as encountered in in-focus star images. For brighter stars, the image typically includes regions above photographic densities where the combined response of the plate and digitizer depends only weakly on the incident flux, i.e. those pixels are effectively saturated. Linearizing the response amounts to stretching out the measured scale progressively towards higher optical densities.

The many approaches to stellar photometry from photographic plates can be generally placed into two categories. In the first, the pixel values within an individual star image are combined to form a measure (or photometric parameter) that is sensitive to the magnitude of the star, and the non-linearity in the flux is accounted for by correcting the photometric parameters to match the magnitudes of calibration stars within the field. Examples of this method include Russell et al. (1990), Lasker et al. (2008), DASCH Laycock et al. (2010), and Sokolovsky et al. (2017). In the second approach, the pixel values are corrected before their summation to form a measure of stellar flux guided by some constraint, for example that the point-spread-function should look the same for faint star profiles and for bright star profiles. This method was explored by e.g. Kroll & Neugebauer (1993), Hambly et al. (2001), Barbieri et al. (2003), and Johnson & Winn (2004). As described in Section 3.2, this paper falls into the second category. We describe a transformation of the original pixel values into values that approximate intensities that accounts simultaneously for the scanner response and the photographic response. As detailed below, we first obtain insight into a suitable transformation equation by utilizing a calibrated step wedge, and then we iteratively refine the two parameters of the transformation equation to find values that approximately linearize the magnitude scale. For simplicity, we use a fixed aperture for the photometry, despite optical aberrations becoming evident for field angles larger than two degrees.

Given the simplicity of the transformation equation, the radial variation of the point-spread function, our use of a fixed aperture, and vignetting, we anticipate that corrections to our magnitudes will be necessary that will depend on both magnitude and field coordinates. For the particular application of measuring or constraining

variability, it is appropriate to measure stars of similar magnitude and field position differentially since they can be expected to all suffer the same systematics. The plate we have chosen for this study has a high surface density of stars, enabling adequate comparison samples for all but the brightest stars.

With this differential approach in mind, the utility of our catalog for long-term variability studies depends on the size of the random errors. Many factors enter into the random errors: image crowding and plate noise, which are intrinsic to the plate; electronic noise and other features that are intrinsic to the digitizer; and parameter choices for the photometry that are under our control. We estimate the random photometric errors from the scatter in the magnitude residuals, assuming that most stars have smaller variability ranges than these. With our digitizer and our plate, we can achieve random errors of less than 0.15 mag, comparable to the efforts mentioned earlier.

This paper is structured as follows. In Section 2, we discuss the plate collection at Yerkes Observatory. We also discuss Barnard's *Atlas* and our reasons for selecting plate "10B-161" for our analysis. In Section 3, we document our process for digitizing the plate using a graphic arts scanner and the specifications of the resulting TIFF file. We also describe the process by which we produce a transformed FITS file for analysis. In Section 4, we detail our method of identifying stars in the plate field and measuring their magnitudes. In Section 5, we investigate the photometric repeatability of magnitude measurement between rotated scans, compare our magnitude measurements to Gaia Early Data Release 3 (EDR3; Brown et al. 2021), and discuss the completeness of our catalog of sources from 10B-161. In Section 6, we use the methods discussed throughout this paper to measure the magnitudes of known red supergiant stars in the field of 10B-161, and the implications of our measurements. Finally, in Section 7, we describe the resultant catalog of 66,000 stars from 10B-161 with their astrometric and photometric measurements; and direct the reader to where this catalog and its source files can be publicly accessed.

2. YERKES PLATE COLLECTION AND PLATE SELECTION

The original plates included in the *Atlas* are part of the Yerkes plate collection, which includes between 150,000 and 200,000 photographic plates (for more details on the collection, see Cerny et al. (2021), hereafter Paper I). Paper I focused on a sky survey plate denoted "Ry60" taken with the Ritchey 24-inch reflector telescope, but our current project focuses instead on the 50

plates in the Barnard *Atlas*. There are several key differences between these plates and Ry60: (1) the plate scale of the Barnard plates (161 arcsec/mm) is smaller by almost a factor of 2 than that of Ry60 (87.4 arcsec/mm), (2) the fields are larger (13.6 degrees on a side for the Barnard plates, compared to 1.8 degrees on a side for the Ritchey plates), (3) the plates are more densely crowded with stars, since they deliberately focus on fields at low Galactic latitudes, and (4) interstellar absorption is significant and uneven in the Barnard survey, whereas such effects were negligible on Ry60. These factors complicate the extraction of accurate magnitude measurements from Barnard's plates, but by no means render them impossible.

From the 50 plates included in the Barnard *Atlas*, we chose Plate 8 (to which we hereafter refer by its series number in Barnard's logbook, 10B-161) for analysis. The full plate scan is reproduced in Figure 1. The catalog which we present later in the paper contains 66,000 stars within the 46-square-degree area that we measured; since our digitization process (see Section 3) cannot resolve stars closer than about 10 arcseconds, this value is a lower limit to the number of stars truly captured on the plate above our magnitude limit. Compared to the other plates in the *Atlas*, the density of stars on 10B-161 is relatively sparse and their distribution is fairly uniform across the plate. The plate is centered near Messier 35 (hereafter M35), a star cluster that could act as a photometric calibrator with existing B-band photometry and spectroscopic data. We explored using these data for calibrations, but finally decided that use of Gaia EDR3 (van Leeuwen et al. 2021) was sufficient, as described below.

The properties of the original negative are summarized in Table 1. The plate encompasses a region in Gemini and has the shortest exposure time of any plate in the *Atlas* at only 50 minutes (Barnard et al. 1927). Barnard notes frankly that, while he did not find the plate particularly interesting (potentially because none of the dark objects included in the Barnard Catalog are present in its field), it did include several features he found worthy of note, namely "dark lanes" obscuring the background star field.

The field of 10B-161 includes the intersection of the ecliptic and the Galactic equators and also appears in the contemporaneous Wolf-Palisa survey of the ecliptic, which used a similar telescope. The Wolf-Palisa plates have been digitized (Mandel et al. 2007) and could provide an interesting comparison, which we leave to future studies. In addition to M35, 10B-161 also includes NGC 2158, a rich cluster immediately to the southwest

Table 1.   A Summary of the Properties of 10B-161

Parameter	Value
Physical dimensions	12 in by 12 in
Center (1875)	6:01:55, +24° 22'
Center (J2000)	6:09:35, +24° 22'
Date of exposure	1905 March 23 03:24 GMT MJD=16927.142
Exposure time	50 minutes
Location	Mt. Wilson Observatory
Latitude	34° 13' N
Altitude	5900 ft (1800 m)
Telescope	Bruce 10-in. refractor
Physical plate scale	161 arcseconds/mm
Sky area captured	13° by 13°
Emulsion	Seed 23
Emulsion sensitivity	Blue 400 - 500 nm
Galactic coordinates at center (l, b)	$(187°, 2°)$
Ecliptic coordinates at center (λ, β)	$(92°, 1°)$
Point-spread function	80% encircled energy within a 10 arcsecond radius

Table 2. A summary of the properties of the 10B-161 scans

Parameter	Value
Physical dimensions	6 in. by 6 in.
Sky area scanned	6.8° by 6.8°
Scan center (degrees)	92.457, +24.482
Dots per inch (dpi)	1200
Step size (microns)	21.2
Step size (arcseconds)	3.4
Color depth	16 bit RGB

of M35, and IC 444, a small reflection nebula particularly remarked on by Barnard.

Our overall approach to the analysis of 10B-161 is to compile measurements of stellar magnitudes derived from plate scans and calibrate them against the astrometry and photometry from Gaia EDR3.

3. DIGITIZATION USING A COMMERCIAL SCANNER

3.1. *Digitization and Astrometric Solution*

As in Paper I, we conducted our digitization process with an Epson Expression 12000XL[3], a flatbed graphic

arts scanner with the ability to scan transmissive media via an accessory transparancy unit. The transparency unit provides an LED light source which feeds into the scanner carriage, passing through the sample once. The detector is described by Epson as a "color CCD line sensor." An analysis of an Epson V750 scanner (an older model but likely similar to the 12000XL) by Simcoe (2009) found a 6-line, 20,400 pixel array with a 16-bit Analog-Digital Converter (see also Shelton (2009)). Simcoe (2009) estimated a full-well capacity of 30,000 to 40,000 electrons for each pixel, corresponding to 8 to 9 bits of data not dominated by noise. We configured our own scanner using the commercial software Silverfast 8 to produce an uncompressed TIFF file with 16 bits per RGB color channel. We made the choice between 16-bits and 8-bits based on the possibility that the 12000XL could produce more than 8 bits of information per pixel.[3] By selecting the "Archive" option in Silverfast, we ensured that no measures were taken by the scanner to alter the pixel values from its otherwise neutral output.

---

[3]   https://epson.com/For-Work/Scanners/Photo-and-Graphics/Epson-Expression-12000XL-Photo-Scanner/p/12000XL-PH

[3] These plates will eventually be incorporated into the University of Chicago's Special Collections, utilized by researchers across disciplines. While the photographic image itself is grayscale, many plates in this collection have red annotations, including 10B-161. We chose to follow the Federal Agencies Digital Guidelines Initiative (2016) which recommends scanning photographic negatives larger than 4-in by 5-in in "Greyscale or Color as appropriate." This led us to scan our materials in RGB.

We made four scans of 10B-161: the central 6×6 inches at 1200 dpi, the entire plate (12 inches) at 600 dpi, the central 6×6 inches rotated 90 degrees at 1200 dpi, and the whole plate rotated in the same way at 600 dpi. We only used the inner six-inch scans in our analysis, and the specifications of these scans comprise Table 2. The larger scans are intended for archival use and to study the annotations around the edges of the plate. By using only the inner part of the field, we remove from our consideration those stars most affected by optical aberrations towards the edges. With the scanner's spatial resolution set to 1200 dpi, stars are sampled by about 5 pixels in one dimension (or 17 arcseconds), which we found to be sufficient for astrometric and photometric measurement (see Table 2). We explored the possibility of scanning 10B-161 at resolutions as high as 1600 dpi, but found that the improvement in the precision of our results was marginal, while the increase in scanning time was quite large. At the same time as these scans were made, and with the same settings employed for the inner six-inch scans, we also scanned a Stouffer 21-step sensitivity guide [4], hereafter referred to as a "step wedge." This step wedge was used to characterize the relationship between the scanner's output and the true densities which the machine would encounter on our plate. The step wedge contains 21 steps beginning with a density of 0.06, increasing in increments of $\sqrt{2}$, and ending with a maximum density of 3.08.

We next prepared our files to receive a WCS TAN+SIP (World Coordinate System TANgent plane projection + Simple Imaging Polynomial) solution by reducing each image's initial file size (about 300 MB) and transforming it into a FITS file. To do so, we used ImageJ (Schneider et al. 2012) to split the color channels, added the channels together after having divided them each by 3.0, and saved the resultant file in FITS form. This produced a single 100 MB grayscale FITS file with the same characteristics as the original TIFF file. The smaller file was then uploaded to `Astrometry.net` to obtain a WCS solution. `Astrometry.net` uses the USNO-B catalog of astrometric standards to create solutions for input files in the J2000 epoch. After one pass through the system, the WCS solution for the inner 6-inch non-rotated scan of 10B-161 contained 40 stars matched to the reference catalog and an RMS residual of 3.797 arcseconds. After a second pass, the solution included 818 matched stars and an RMS residual of 3.602 arcseconds. A third pass through the software also included 818 matched stars and an RMS residual
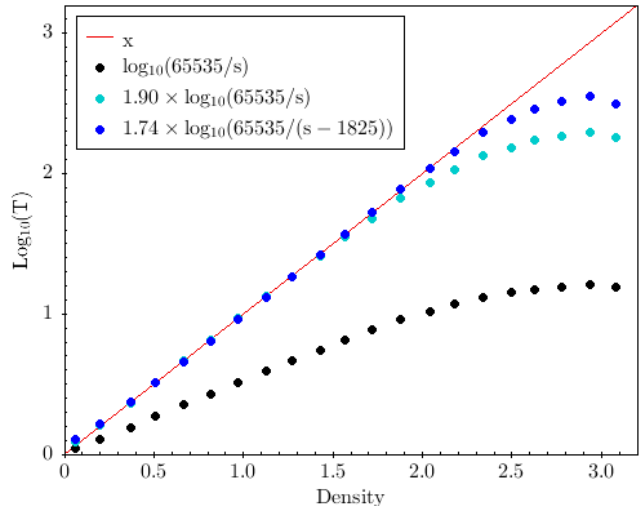
Figure 2. The mean values returned by the Epson 12000XL scanner for each step on a Stouffer 21-step wedge, transformed in three consecutive stages to approximate the true photographic density on the step wedge.

of 3.602 arcseconds, providing no further improvement upon the previous pass. Therefore, we settled on two passes through `Astrometry.net` as ideal for our purposes.

3.2. *Photometric Transformation*

Two factors determine the relationship between the incident intensity at different locations on the plate surface and the corresponding output of the scanner at those locations. First, the Seed 23 emulsion on which the image was captured did not have a linear relationship with the magnitudes of the stars to whose light it was exposed in 1905. Second, the output of the scanner does not correspond linearly with the plate density. In Paper I, we derived a function which allowed us to accurately model the conversion from scanner output to plate density within a limited range. In this work, we experimented with altering both the parameters and functional form of our Paper I transformation. Our initial transformation experiment was as follows:

$$T_{initial} = \left[\frac{65535}{s} \right] \qquad (1)$$

Here, $T_{initial}$ represents the transformed value, 65535 is the maximum scanner output value, and s represents the original scanner output value.

Figure 2 shows the photographic density of our test step wedge plotted against the scanner output when transformed according to each stage of our optimization process. The set of data represented by black dots shows the log of the scanner output when transformed simply by Equation 1, a result very similar to the step

wedge plot in Shelton (2009), albeit for a different scanner. At this stage, the relationship between output and density did not have a unit slope anywhere along its range. We corrected for this with a multiplicative factor, which yields a unit slope within the density range 0.37 to 1.57. We continued to modify the equation to produce our final form, which included (1) a multiplicative factor (1.90 in the turquoise dataset and 1.74 in the blue dataset displayed in Figure 2), and (2) an offset to the scanner output (equal to 1825 in the blue dataset). This final alteration allowed us to accurately measure densities between 0.37 and 2.18. Beyond a density of 2.18, the linearity of the relationship begins to fail. At a density of around 2.94, the scanner measures increasing densities to be smaller than those which preceded them. This may be due to light within the scanner reflecting off of the darkest portions of the step wedge, and therefore we discount measurements past this point.

The general form for our transformation is below (see Equation 2.) P_1 is the parameter responsible for initially setting the slope equal to 1; P_2 is an offset parameter; and C is a scaling factor. Except for the P_2 parameter, this relation is the same as Equation 1 of Hambly et al. (2001). As already mentioned, the transformation is intended to account for both the photographic intensity-to-density relation and the density-to-scanner-output relation.

$$T_{general} = C \times \left[\frac{65535}{s - P_2} \right]^{P_1} \qquad (2)$$

Having arrived at a satisfactory form for our transformation based on Figure 2, we engaged in a long period of trial and error to find the ideal parameter values to model the stellar magnitudes captured on 10B-161. Our goal was to model stellar magnitudes from our test plate over as great a range as possible without requiring a physical justification for the mathematical features of our transformation. We neither attempted rigorous optimization nor explored the application of our equation to other plates, efforts we reserve for future works. The final transformation equation (see Equation 3) includes a scaling factor with a value of 86.0; P_1 equal to 1.75; and P_2 equal to 6000.

$$T_{final} = 86.0 \times \left[\frac{65535}{s - 6000} \right]^{1.75} \qquad (3)$$

We transformed each pixel value in the two FITS files (original version and 90-degrees-rotated version) according to the above equation, maintaining 16-bit integer precision. The value for the scale factor ($C = 86$) was chosen so that pixels near the level of the sky background would have values large enough to resolve the

noise, while being small enough to enable much brighter regions to fit within the 16-bit range.

4. ASTROMETRY, PHOTOMETRY, AND CREATION OF STELLAR CATALOG

4.1. *Measurement of Plate Magnitudes*

To identify sources in the field of 10B-161, obtain their right ascension and declination, and measure their magnitudes, we opened our transformed FITS file in the `Aperture Photometry Tool` (APT; Laher et al. 2012). We chose to use APT because it is designed to encourage inspection of the image (e.g. to identify neighboring stars that may be close to the measurement aperture), and provides extensive visual tools which enable good choices in establishing the values of the measurement parameters. This is particularly useful when working with a crowded field of stars. APT is capable of both creating its own source lists and of evaluating magnitudes at coordinates given by an external catalog. For this work, we used the latter option by creating a list of stars within the field of plate 10B-161 from Gaia EDR3, along with their projected positions in 1905 calculated using Gaia's proper motions. The formulae for these projections are shown below, where R.A. and Decl. are given in degrees and $\mu_{\mathrm{R.A.,2016}}$ and $\mu_{\mathrm{Decl.,2016}}$ are given in milliarcseconds per year.

$$\mathrm{R.A._{1905} = R.A._{2016}} - \frac{\mu_{\mathrm{R.A.,2016}} \times 110.8}{1000 \times \cos(\mathrm{Decl._{2016}}) \times 3600} \qquad (4)$$

$$\mathrm{Decl._{1905} = Decl._{2016}} - \frac{\mu_{\mathrm{Decl.,2016}} \times 110.8}{1000 \times 3600} \qquad (5)$$

The input list was limited to stars with a magnitude *pg* < 16.9 mag (the definition of *pg* is given in Section 5.2). APT has an operational limit of 100,000 sources per run and the Gaia catalog includes just under 100,000 stars with *pg* < 16.9 mag within our field.

To determine magnitudes, APT places a fixed aperture on each source and subtracts the sky background. The aperture is automatically shifted to the centroid of the light within a specified distance. We performed a series of APT runs with different aperture and centroid radius values to determine what settings provided the best magnitude measurements from the stars on our plate. In the end, we chose to move forward with an aperture radius of 3 pixels (10 arcsec) and a centroid-centering radius of 3 pixels.

We input the list of positions to APT and produced a table of magnitudes at those positions based on the transformed image files as described in Section 3. We repeated this process on our 90 degree rotated scan of
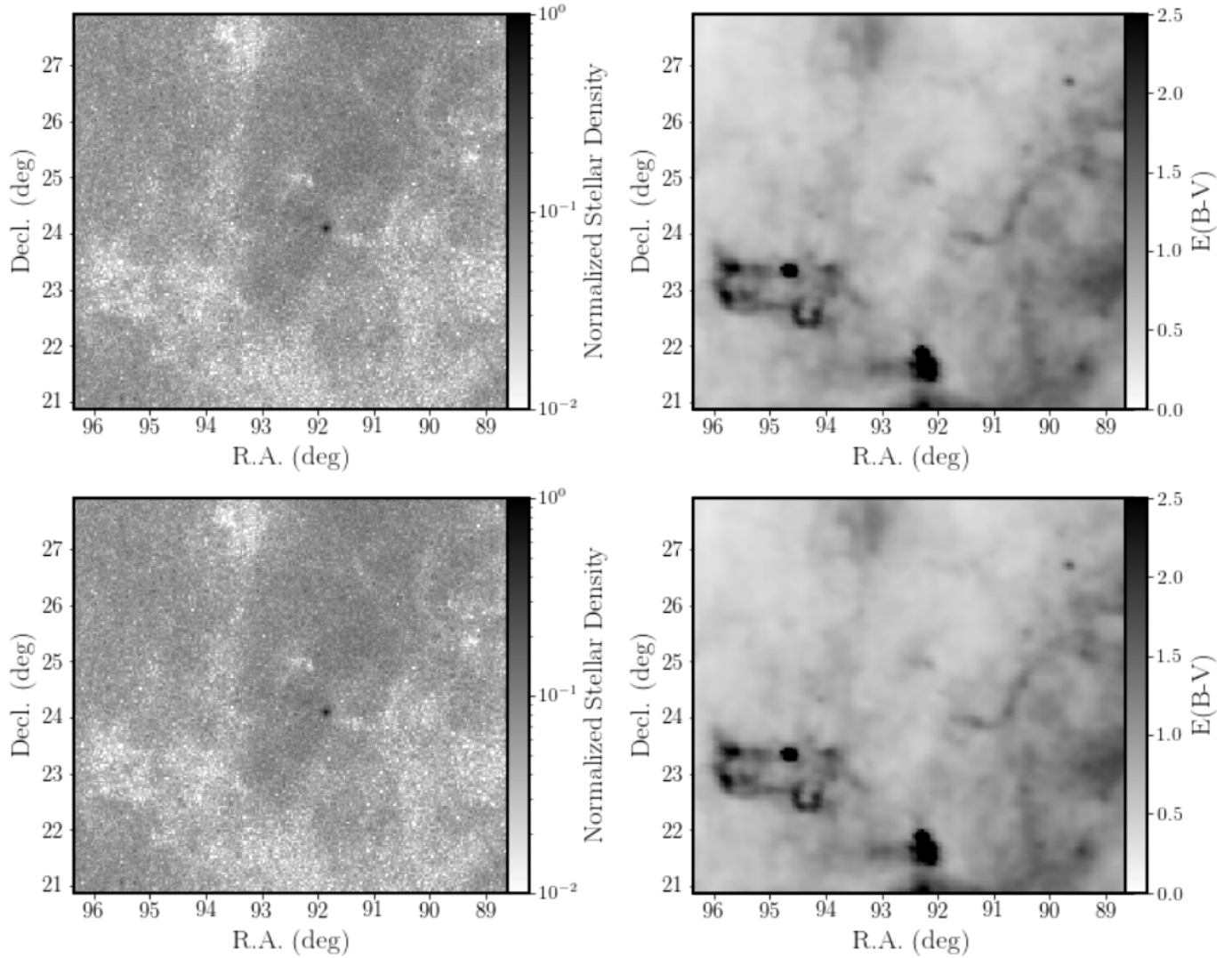
Figure 3. (Left) Stellar density map for the 10B-161 field, including only sources that matched between our plate catalog and Gaia. The small high-density knot near the center is NGC 2158. (Right) Map of $E(B-V)$ reddenings for the same field, as measured by Schlegel et al. (1998). In general, we find the expected trend that regions of higher dust extinction correspond to regions with fewer matched sources.

the plate in order to analyze both the astrometric performance and photometric repeatability of our results.

Within the central field of the plate, the 3-pixel-radius aperture captures about 80 percent of the light, with a progressively smaller fraction of the light included within the fixed aperture towards the edge of the field because of optical aberrations. The background sky level was determined with APT's "non-sky-annulus local mode subtraction" option that seems to be the least biased by light from neighboring stars. The faintest stars in our catalog are measured to have approximately equal flux from the star and from the sky within the 3-pixel radius aperture.

4.2. Nebulous Objects

In the left-hand panel of Figure 3, we display a map of the resulting source catalog, including only identified stars that matched with Gaia EDR3 within a 10 arcsecond separation. In the right-hand panel, we include the corresponding dust map (in terms of $E(B-V)$ color excess) for the same region from Schlegel et al. (1998). As the juxtaposition of these figures reveal, and as originally noted by Barnard, nebulous regions with high dust extinction result in significant variation in the stellar density as a function of position. The smaller features in the reddening map correspond to infrared sources that are not as obviously correlated with interstellar extinction. The blob near the southern edge of the field is the HII region coincident with the radio source PKS 0605+21. It appears as a low-surface-brightness patch

at red wavelengths and it is invisible on 10B-161. It has been classified as an H II region by Sharpless (1959) (his No. 247) but the ionizing stars are not apparent. The arc in the map is IC 443, a supernova remnant that is visible on 10B-161 but not remarked on by Barnard. To its northeast is IC 444, a reflection nebula associated with the B9 star 12 *Gem* that Barnard calls "nebulous." The diffuse emission in the dust map to the east of IC 444 and IC 443 corresponds to Sharpless 249, an extended ionized region.

4.3. *Astrometric Performance*

In order to determine the quality of astrometric measurement produced by our methods, we turned to the Tool for OPerations on Catalogues And Tables (`TOPCAT`; Taylor 2005). Using its match function, we matched the catalogs derived from 10B-161 with our Gaia catalog. The match of a measurement on 10B-161 is not necessarily with the same star in the Gaia catalog that was used for placing the aperture because APT recenters on the centroid of the star image.

Our matched tables included the R.A., Decl., and magnitude values from both the Gaia catalog and APT, and allowed us to explore the errors in R.A. and Decl. across the plate. As noted in Paper I, and as seen in Figure 4, the scanner introduces irregularities that appear most prominently as quasi-periodic residuals in the coordinate oriented in the scanning direction (see also Vicente et al. 2007; Pakuliak et al. 2011). To correct approximately for these errors, we matched a sine function to the residuals by eye to reduce the extrema (see the far left panels of Figure 4).

We took these approximate corrections and applied them to the original (unmatched) tables derived from APT, producing the lower-amplitude residuals seen in the center-left panels. We then matched the two perpendicular scans of 10B-161 with each other, again using the TOPCAT match function and the corrected coordinates. This new, corrected catalog was finally matched with Gaia, using the coordinates with the smallest residuals from each scan (R.A. from the non-rotated scan and Decl. from the rotated scan.) The corresponding residuals are shown in the center-right panels of Figure 5.

After applying these corrections, the median angular separation between our plate position measurements and Gaia EDR3 was 1.37 arcseconds over 66,000 matched sources, representing a significant improvement in the astrometric precision of our catalog (Figure 5). Taking the best coordinate from each of the two perpendicular scans is another innovation over Paper I. We emphasize that the main motivation for improving the astrometric

precision is to improve the reliability of the association of stars in our catalog with stars in Gaia EDR3.

4.4. *Diffuse Light: Vignetting and Scattering*

Diffuse light within the field is automatically subtracted from the aperture measurements, and its variation across the field is not clearly apparent in our photometric residuals. Optical vignetting results in less light received from stars at large field angle, and similarly from the sky background which can be a proxy for vignetting. The combination of plate scale, image size, and star density in our field is such that scattered light from stars contaminates many of the measures of sky background, but the lower envelope of sky background versus field angle should reflect the underlying trend. Figure 6 shows this effect, where the lower envelope decreases by about 9 percent from center to edge. At a field angle of two degrees, the spread in the pixel values has a similar range, i.e. the effect of vignetting has an amplitude that is comparable to other variations in the sky level.

To investigate the effect of light scattering to large angles, we chose one of the brightest stars in the field, η Gem ($B = 4.9$), and plotted individual pixel intensities as a function of radial distance from the star (Figure 7). The star itself is off-scale at the extreme left. The pixels above the main trend line are affected by other stars in the neighborhood, but the lower envelope should approximate the outer profile of η Gem, which is clearly detected past 5 arcmin.

5. PHOTOMETRIC CALIBRATION AND PERFORMANCE

5.1. *Photometric Repeatability*

In order to quantify the effect of plate orientation on the scanning process and the repeatability of our results between plates scanned at different times, we refer to our rotated (90 degree) and non-rotated (0 degree) FITS files of 10B-161, following the procedure of Vicente et al. (2007) and Pakuliak et al. (2011). The two scans were made 12 days apart and with different room illuminations. In principle, the difference in ambient illumination could affect repeatability. Moreover, the scanner could have intrinsic variability week-to-week. The average difference between the magnitude measurements of the two scans is about 0.09 mag and is approximately independent of the image's true magnitude. After removing this offset, we average the two measurements (hereafter *mag*) and also record the difference (Δmag). Neglecting the brightest and faintest stars, the root-mean-square scatter of Δmag is about 0.04 mag.
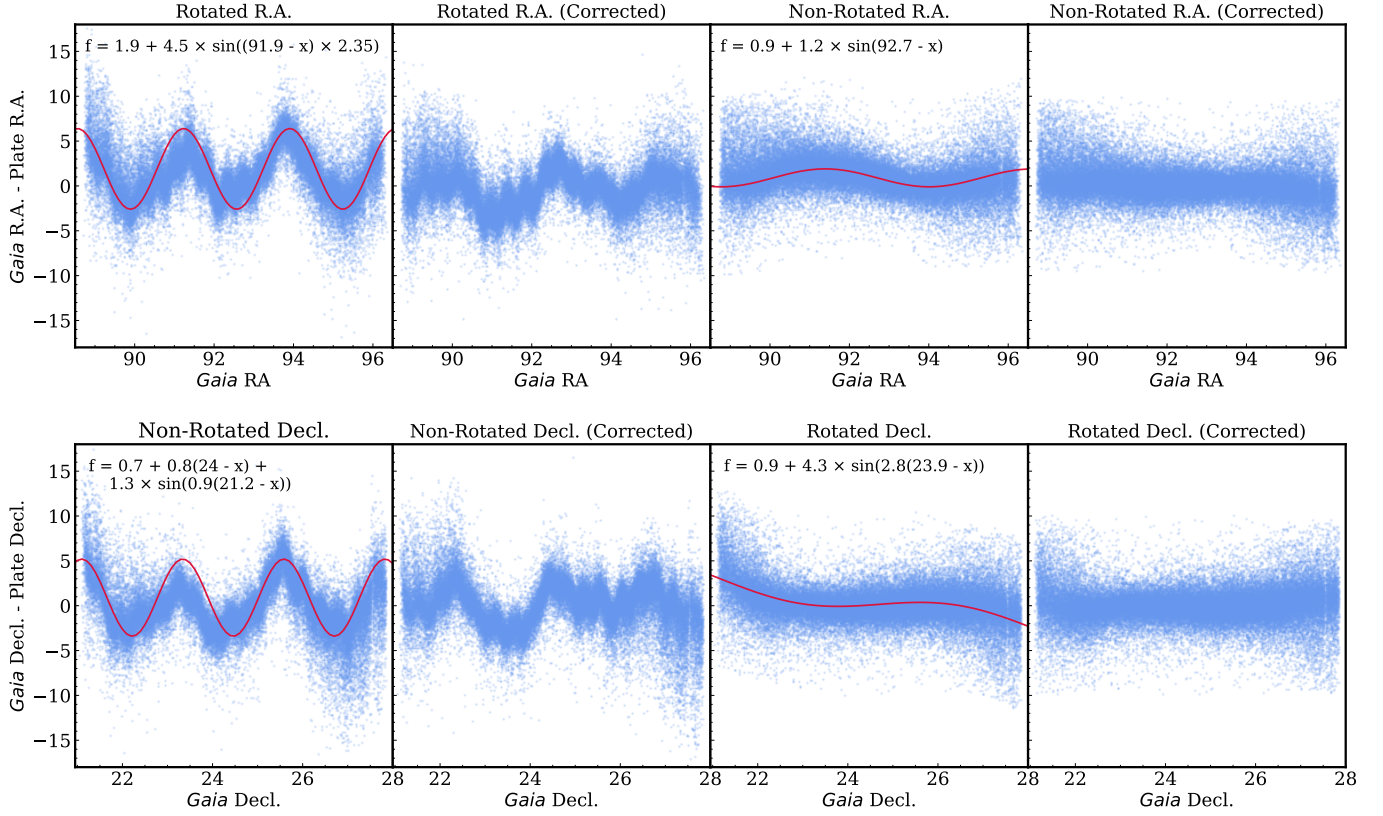
Figure 4. Astrometric residuals compared to Gaia, depicting the multi-step progression detailed in the text. The curves displayed on the uncorrected residual plots are the sine functions used to create the corrected residuals displayed beside them. For our catalog, we used the corrected R.A. values from the non-rotated scan and the corrected Decl. values from the rotated scan. The residuals of these data are shown in the rightmost plot of each row.
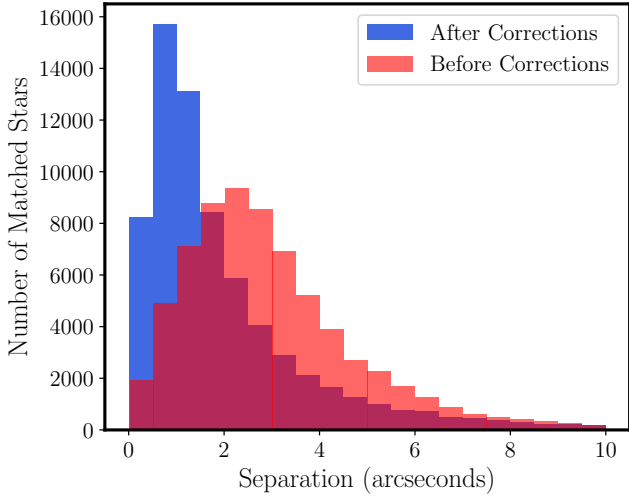

Figure 5. Angular Separation of sources matched with Gaia EDR3. In red, we show the histogram of separations from the original non-rotated scan, with no corrections applied to account for the quasi-periodic residuals introduced by the scanner. In blue, we show the same histogram after applying the correction procedure described in the text.
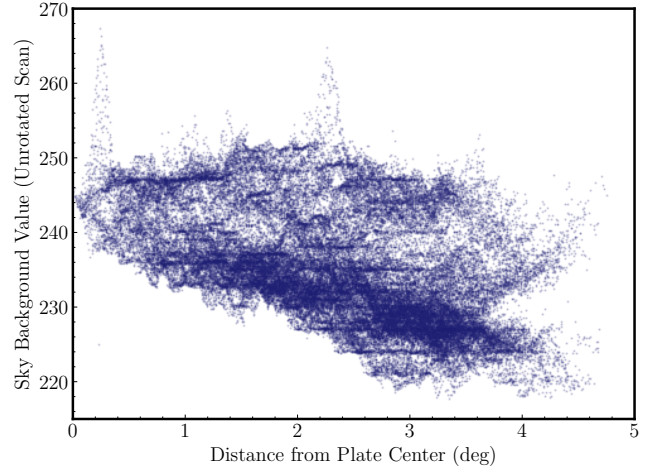
Figure 6. Sky brightness measurements as determined by APT for each star as a function of radial distance from the field center.

After recording the 0.09 mag offset between our two scans we decided to conduct further testing on our scanner's repeatability and precision. To do this, we took scans of the step wedge over the course of 12 days with-
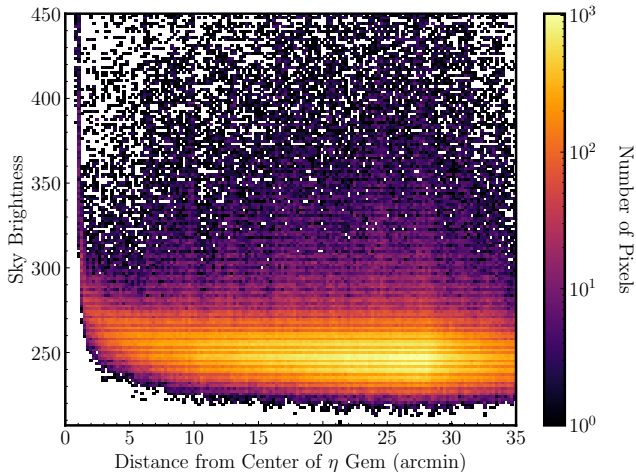
Figure 7. Sky brightness in each pixel as a function of distance from the bright star η Gem.
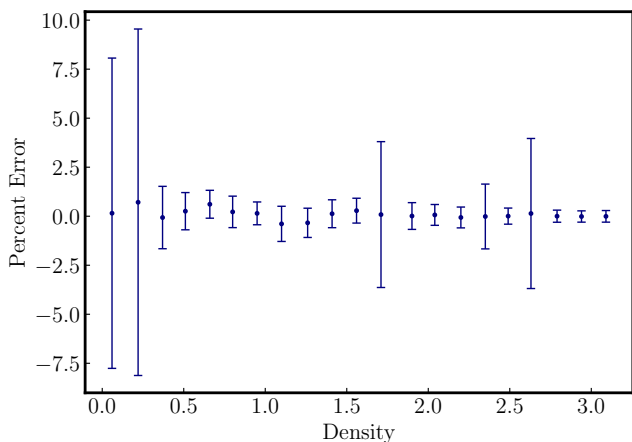

Figure 8. Test for repeatability of the scanner over a 12-day trial using the step wedge, where the x-axis shows the 21 steps. In a region within each step, the corresponding pixels were subtracted from each other. The dots are the mean residuals and the bars are the standard deviations of the pixel values expressed as percentages. Larger bars indicate steps that included blemishes.

out moving the step wedge or scanner, i.e. a time interval that matched the interval between the original non-rotated and rotated scans of 10B-161. After subtracting the step wedge scans from each other on a pixel-by-pixel basis, we looked at the difference parallel to the scanning direction to track fluctuations. We learned that the scanner shifts by 1-6 pixels in each axis. We shifted the positions in relation to each other to find the smallest mean difference, as that would imply the scans are aligned and we are comparing the correct corresponding pixel values. Over the course of the 12-day trial, we found that the scanner varies by 0.1 to 7 scanner units (see Figure 8). The scans 12 days apart had a

mean residual of 0.20 percent before accounting for the 1-6 pixel positioning difference. After adjusting the position of the scans we found a mean residual of 0.00031 percent, which is negligible. Tests with different ambient lighting did not result in differences larger than those shown in Figure 8. In summary, the 0.04 mag root-mean-square scatter in the magnitudes measured from the two perpendicular plate scans is, according to this test, much larger than what we found from the step wedge. We conclude that most of the photometric error is due to noise intrinsic to the plate and to the independent placement of the apertures on the star images.

5.2. *Photometric Calibration*

The transformation of the scanner output adopted in Section 3 results in aperture measurements that differ from a linear magnitude system, depending on both magnitude (our simple two-parameter transformation does not capture all effects) and on radial position (optical aberrations and vignetting).

We used stars near the center of the field and at intermediate magnitudes to establish the default photometric zero-point for the catalog. The photometric band is defined by a blue-sensitive emulsion without a filter. The transmission through the lenses likely limits the band at the blue end, and the emulsion sensitivity limits the band at the red end. We estimate the bandpass to cover roughly 400 - 500nm. The stellar population in the field is heavily affected by interstellar reddening, which modifies the effective wavelength appropriate for any given spectral type.

To obtain a photometric zero-point for the magnitude system that is native to the photographic plate, we need to correct for the difference in our effective bandpass with respect to the bands of the external catalog, namely the Gaia bp magnitude and Gaia $bp-rp$ color. Following the practice of Russell et al. (1990) in their Equation 1, we used a simple relation

$$pg = bp + \alpha \times (bp - rp), \qquad (6)$$

where pg is now the estimate of the photographic magnitude based on Gaia photometry. We solved for the value of α that minimized the dependence of $pg - mag$ on $bp-rp$, (which in turn minimized the scatter in other relationships such as $pg-mag$ vs. pg). We found $\alpha = 0.9$ works well across all values of $bp - rp$, indicating that a higher-order color term is not justified. In Paper I we adopted the same approach, but found $\alpha = 1.1$. This difference could be the result of different transmissions of the telescope: the Ritchey telescope, which captured the plate analyzed in Paper I, was a reflector, whereas the Bruce Telescope was a refractor. If the
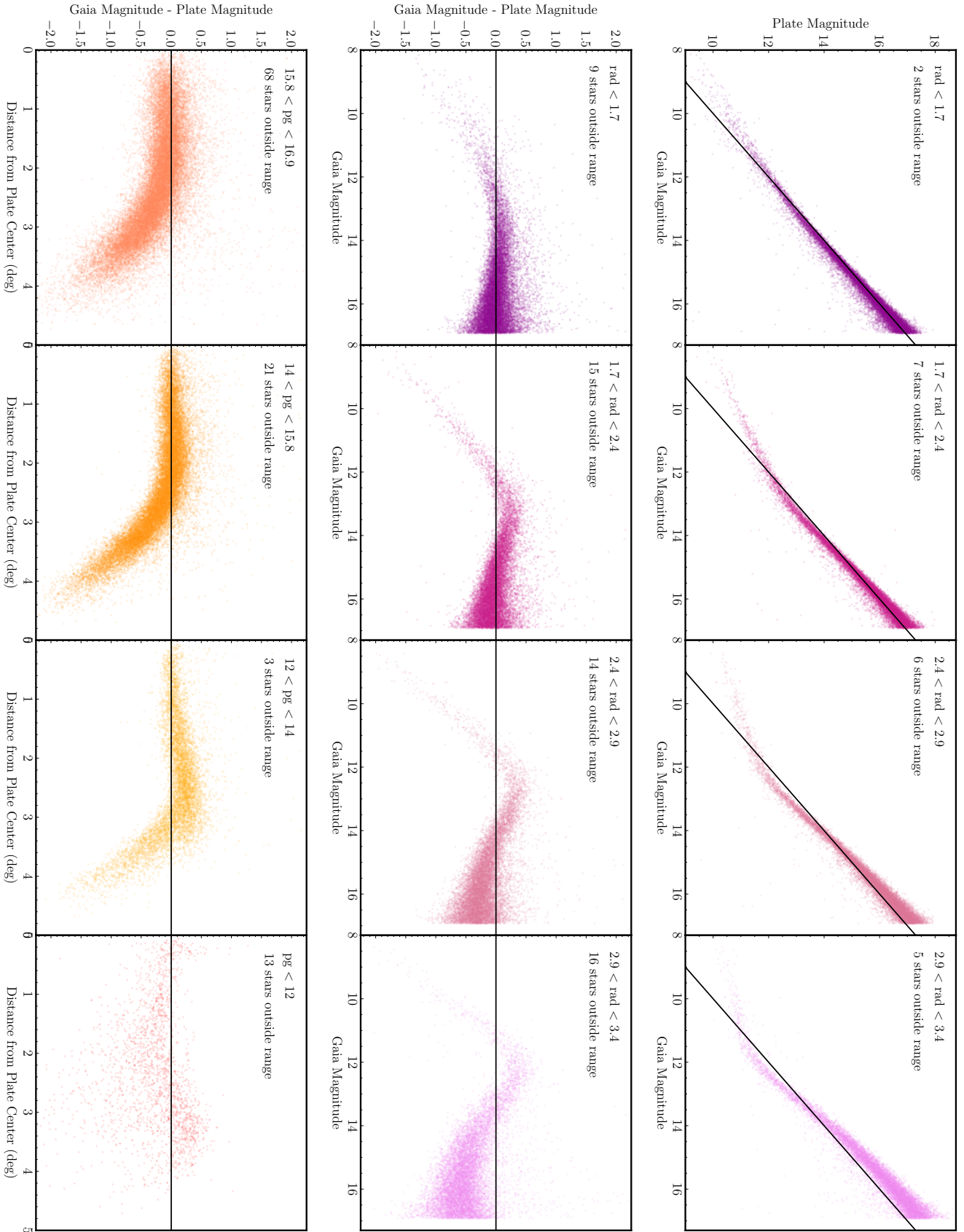
Figure 9. The components of this figure are oriented such that the "upper" four plots are on the right and the "lower" four are on the left. The "upper" four plots show the Gaia *pg* magnitude value on the x-axis compared to the magnitudes found in our final catalog, binned by radial distance from the center of the plate. The "middle" four plots show the residuals associated with these bins. The "lower" four show the magnitude residuals binned by magnitude.

reflector transmitted more light at shorter wavelengths than the refractor, then its band would have a bluer effective wavelength, which would make the corresponding value of α larger (i.e., farther from the Gaia bp band). The differing α values could also have resulted from the two plates having had different emulsion properties or observational conditions (differing airmass, atmospheric absorption, and reddening coefficient could all have contributed.)

Given this formula, we determined the photometric zero-point from the stars near the field center, as mentioned earlier. Figure 9 shows an example of the residuals. The solid black line is our default zero-point calibration. Within a radial distance of 1.7 degrees, our measurements are close to linear for $pg > 14$, but in detail our magnitude measurements do depend on magnitude and radial distance as shown in Figure 9. Figure 10 shows measured photometric residuals as a function of sky position, with bluer and redder points corresponding to overestimated and underestimated magnitudes as compared to Gaia, respectively. Within 1.7 degrees of the plate center, ninety-six percent of stars are measured within half a magnitude of the transformed Gaia measurement. For the subsample illustrated in Figure 9 defined by radius < 1.7 degrees and $14 < pg < 15.8$, the standard deviation in our measurements is 0.15 mag, after removing 2 percent of the stars with 3-σ clipping on the quantity $pg - mag$.

5.3. *Catalog Completeness*

In order to quantify the completeness of our catalog, we determined what fraction of stars seen by Gaia appear in our own. To do this, for each of the four bins used in Figure 9, we compared the number of stars detected on our plate with APT and the number of stars detected by Gaia. A comparison between these samples allowed us to investigate the completeness of the plate as a function of radial distance from the center. For the outermost bin, we shrank the maximum radial distance from 3.4 degrees to 3.25 degrees to discount the areas covered by marker in Barnard's plate annotations, as we found these areas to have a non-negligible effect on our completeness results when included.

Due to optical aberrations the star images on the plate are distorted slightly, with the effect being greatest near the edges of the field. As a result of this elongation, the flux of the star within a fixed aperture decreases as radial distance from the plate's focal center increases. As shown in Figure 10, this effect is minimized for stars within about 2.4 degrees of the focal center, and becomes greatly pronounced at larger radial distances. As a result, the detectability of the faintest stars drops with

greater radial distance. Moreover, certain bright stars stars may be missed in our catalog as well. These stars are highly saturated and the resulting large area of the stellar images can result in identification of a center that is far from the correct position (our nominal maximum distance for matching between the APT measures and Gaia is 10 arcsec).

These effects can be seen in Figure 11. The completeness depends more on magnitude than on radial distance, with the catalog recording a smaller percentage of the brightest and faintest stars when compared to intermediate magnitudes. For pg magnitudes between 10 and 15, the inner three radial bins had a completeness ranging from 92-93 percent while the outer bin was only at 90 percent. For the faintest magnitude bin (magnitude range of $16.5 - 16.9$), the three inner regions surveyed had a percent completeness between 71-74 percent, while the outer region's completeness dropped to about 63 percent. Due to the small number of bright stars, it is difficult to make a statistically sound assessment of their completeness.

In summary, the original Gaia source list within 3.25 degrees from our focal center comprised slightly fewer than 66,000 stars, and our catalog within the same area consists of around 53,600 stars. This difference is due to a number of factors, including (1) some faint stars are below our chosen threshold because the subtracted sky background had been overestimated, (2) faint stars proximate to brighter stars are likely to be missed, (3) optical aberrations towards the edges of the plate field render star images more difficult to identify, and (4) the vignetting effect which causes less light to reach the corners of the plate than the focal center.

6. SUPERGIANT IDENTIFICATION AND MAGNITUDE MEASUREMENT

To illustrate the catalog's utility for scientific research, we apply it to the problem of long-term stellar variability. Measurements on historic plates such as 10B-161 can provide the data necessary to confirm variability on the time scale of a century, thus extending light curve data and potentially resulting in more accurate period measurements. An earlier study, Kiss et al. (2006), analyzed photometric measurements spanning an average of 61 years for a sample of 48 red supergiants to explore periodicities in their light curves, confirming variations on time scales of years. To study similar long-period variables on 10B-161, we cross-matched our catalog stars with the red supergiant candidates listed in Messineo & Brown (2019) (hereafter MB19). This catalog consists of 889 bright, K-M Type I stars at low Galactic latitude sourced from prior publications in the field in tandem
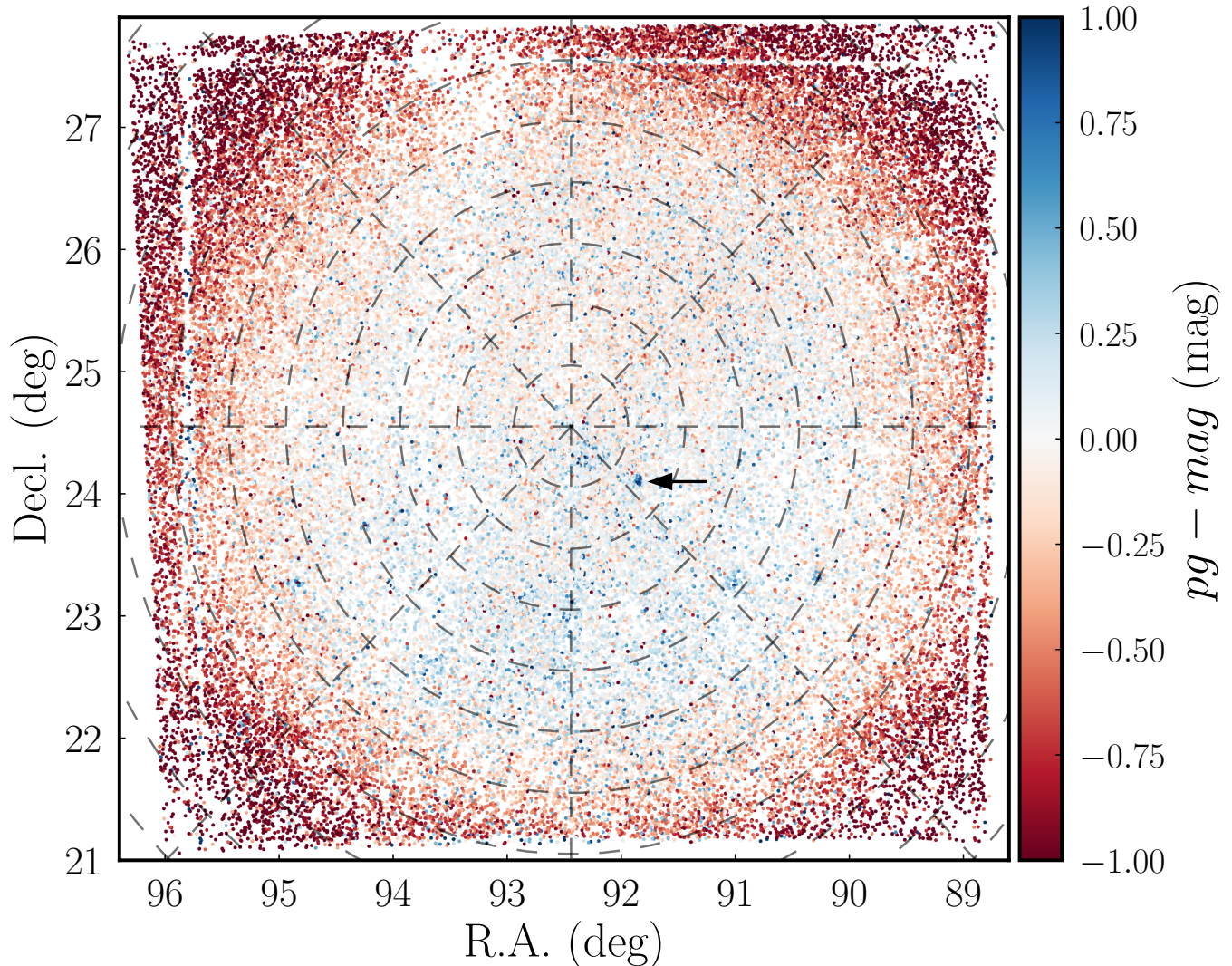
Figure 10. Magnitude residuals as a function of on-sky position for all matched stars in the scanned area of the plate. Dotted lines are plotted on a polar grid with 0.5 deg. radial resolution and $\frac{\pi}{4}$ angular resolution. The dark blue dot to the lower right of the plate center (indicated by the black arrow) coincides with the compact open cluster NGC 2158. The inaccurate magnitude measurements in this area are likely a result of crowding within the cluster. This plot shows that the photometric residuals across the field are mostly radial.

with measurements in Gaia DR2. Cross-matching our plate's catalog with MB19 yielded nine total matches (see Figure 12), none of which are fainter than our magnitude limit. Following the creation of this nine-star catalog, we initially inspected each by eye (an inconvenient process to perform on the entire plate catalog, but reasonable for this small sample set). Visual inspection of each candidate red supergiant was crucial to better understand issues such as image overlap (this was the case for Star 7 in Figure 12 and its problematically close companion star). Further inspection identified stars too bright for our method of measurement (e.g., Star 9 in Figure 12).

To explore potential variability in the sample of nine red supergiants, we defined a comparison sample of stars that has similar *pg* magnitude and similar radial distance from the center of the plate, where the ranges of magnitude and radial distance were chosen to yield enough stars to provide a good basis for comparison. Having similar radial distance ensures similar vignetting and image structure, an assumption that is justified by the radial symmetry seen in Figure 10. To suppress the effect of position-dependent variations, Innis et al. (2004) adopted a comparison sample of nearby stars for their study of CF *Octantis* across several epochs, and Kolesnikova et al. (2008) divided their field into many subfields. Tang et al. (2013) also demonstrated im-

Table 3. Table of Red Supergiant Candidates in the Field of 10B-161

No.	R.A.$_{\text{J2000}}$ (deg)	Decl.$_{\text{J2000}}$ (deg)	pg (mag)	offset (mag)	offset error	SIMBAD Identifier
1	89.86814	23.75454	13.23	-0.14	0.15	BD+23 1138
2	90.04546	25.57805	14.68	0.13	0.13	GSC 01868-00074
3	90.35624	22.11216	13.00	0.04	0.15	TYC 1325-718-1
4	92.19908	25.64538	10.02	0.22	0.14	V* OX Gem
5	92.25563	23.87295	12.11	0.08	0.13	TYC 1877-1668-1
6	92.38512	22.19025	7.88	-0.43	N/A	HD 42049
7	92.93977	23.03015	11.24	0.14	0.16	HD 253017
8	92.98438	23.20705	9.81	0.50	0.14	WY Gem
9	93.71907	22.50675	5.49	...	N/A	η Gem

NOTE—Stars are ordered by increasing Right Ascension. Small cutout images of each star as seen on
the plate are visible in Figure 10, numbered following this scheme. In the text, stars are referenced
by their row value.

proved photometric residuals when comparing stars of similar magnitude in similar regions of the plate, including radial zones as we do here. Since there are relatively few bright stars, this approach becomes less precise for some of the stars in our sample, and Star 9 and Star 6 are so bright that they cannot be measured in this way.

For each of the remaining seven stars, we created a residual plot ($pg - mag$ versus pg) for each respective sample of comparison stars. The trend was fit by eye with a linear term in pg and subtracted to create values on the y-axis with mean equal to zero and no evident trend. In this way, the samples shown in Figure 13 determine both the offset of the measurement of each red supergiant with respect to the mean, as well as the standard deviation within the comparison sample, which we take to be the error of our measured offset after a 3-σ clip. The values of the offset and the standard deviation are entered into Table 3, where positive values indicate the red supergiant was brighter in 1905 than measured by Gaia.

The sample of red supergiants has offsets of typically ± 0.15 mag (see Table 3), which is close to the standard deviation and thus not significant. However, Star 8 was 0.50 mag brighter in 1905, which is more than 3 standard deviations away from the mean of the comparison sample. Star 8 is in fact a known long-term variable red supergiant, WY Gem. According to Kiss et al. (2006), WY Gem has a fundamental period of 353 ± 24 days and a visual-band light curve amplitude of 0.50 mag. Other than WY Gem, only two other stars (OX Gem and η Gem) are included in the General Catalogue of Variable Stars (GCVS Samus et al. (2017)). The entries for all

three stars in the GCVS indicate a variability range of about 1 magnitude.

7. DATA AVAILABILITY AND A USER'S GUIDE TO THE CATALOG

The files used in this research (Glusman et al. 2022) are available to the public via the Knowledge@UChicago Database[2]. These files include the rotated and non-rotated full TIFF scans of 10B-161 (with and without the step wedge used in the calibration process); the rotated and non-rotated center TIFF scans, and their corresponding untransformed FITS files; TIFF scans of the front and back of the envelope used to store the plate; various README files; and finally the catalog used for the analyses described throughout this work. This catalog comprises astrometric and photometric measurements from 1905 of more than 66,000 stars in a 6.8-degree field in the anticenter direction of the Milky Way. Most of the stars have values between 12 and 17 in photographic magnitude.

As described in Section 5.2, the as-measured magnitudes depend on radial position on the plate as well as on magnitude (see Figure 9.) Rather than attempt to correct for these two effects, our catalog provides the magnitudes as measured, using a photometric zero-point based on stars within 1.5 degrees of the center and with $14.5 < pg < 15.5$ mag. The magnitude system is such that a star with measured Gaia $bp - rp = 0.0$ has $mag = pg$. The catalog gives the mean and the difference between the magnitudes in the two perpendicular directions. The
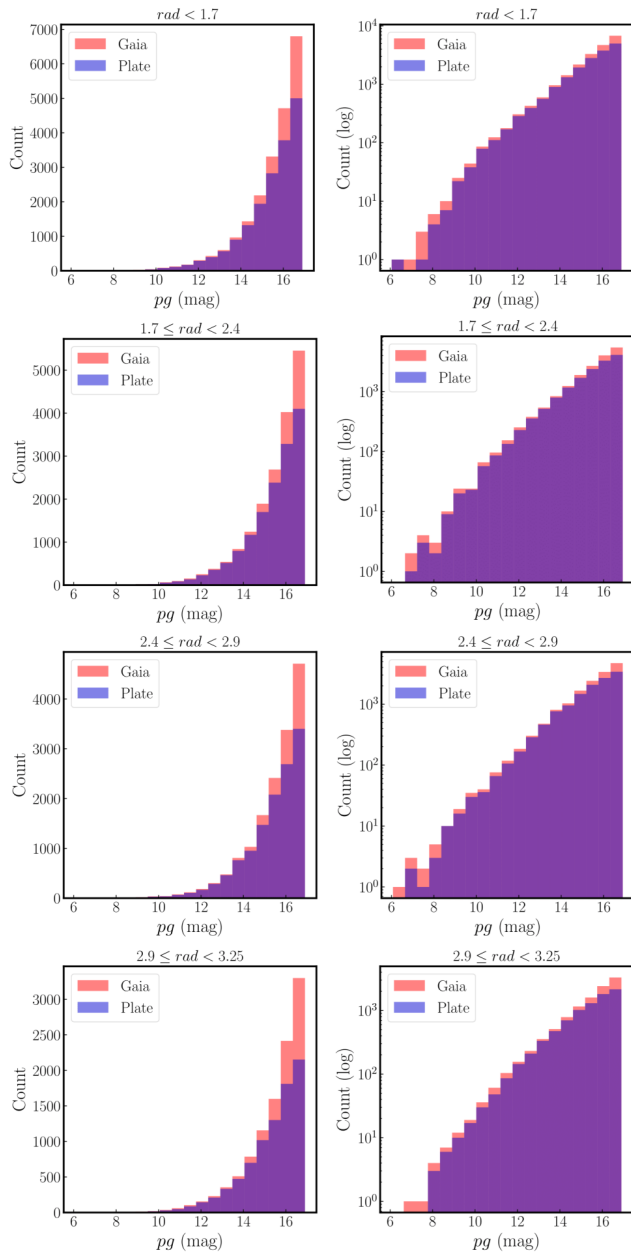
---

[2] https://knowledge.uchicago.edu/

Figure 11. Overlapping histograms showing the total number of stars captured on our plate compared to the total number of stars in the Gaia catalog for this area of sky. Each pair of linear and logarithmic histograms represents a unique radial area in degrees from the focal center of the plate.

catalog's photometric measurements should be used in a comparative sense, namely a star of interest is compared to others of similar magnitude and radial position on the plate, as illustrated in Section 6. Figure 9 illustrates the general level of the gradients to guide the choice of the ranges of magnitude and radius for the comparison sample.
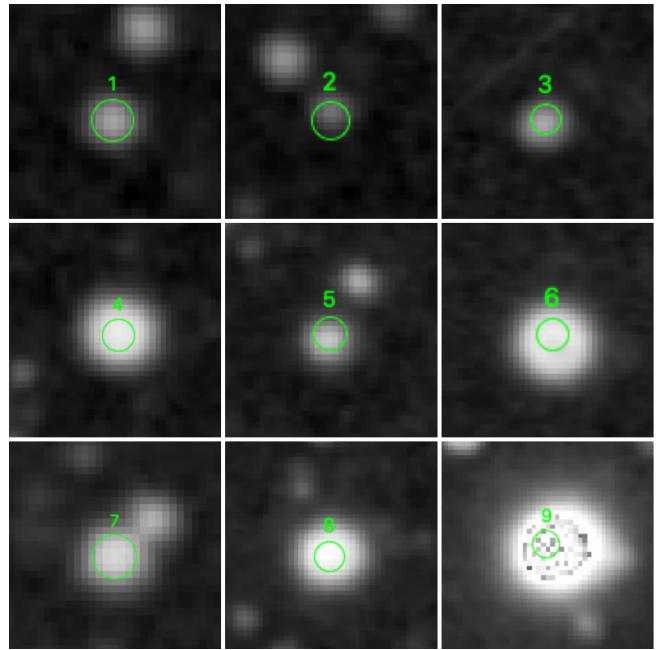
Figure 12. Cut-out images of the stars in common with the MB19 catalog of red supergiants, ordered by increasing R.A. The green circle is the 3-pixel-radius measurement aperture. Star 9 (η *Gem*) shows the effect of central values exceeding the 16-bit limit.

The positions (called "ra_b" and "dec_b" in our catalog) have a median difference with respect to Gaia of about 1.4 arcseconds. These positions are included in the catalog to provide a way to check our match to Gaia, but should be interpreted cautiously due to inference from neighboring stars. For purposes of matching with other sources, the Gaia coordinates (R.A., Decl.) should be used (also given in the catalog for convenience).

8. CONCLUSION

In this work, we have continued our study of extracting scientifically useful data from astronomical photographic plates. As in Paper I, we digitized our research plate of choice using a commercially available scanner and readily available tools. We concentrated our present study on plate 10B-161, taken in 1905, from E. E. Barnard's *Photographic Atlas of Selected Regions of the Milky Way*. All supporting files relevant to our work (including plate scans and our final catalog) have been made available to the public. The catalog includes 66,000 measurements of stellar position and brightness from 117 years ago.

Compared to our initial study in Cerny et al. (2021) (Paper I), we have improved our methods for extracting and manipulating astrometric and photometric data from survey plates. Specifically, we have now incorporated the use of perpendicular scanning to explore and
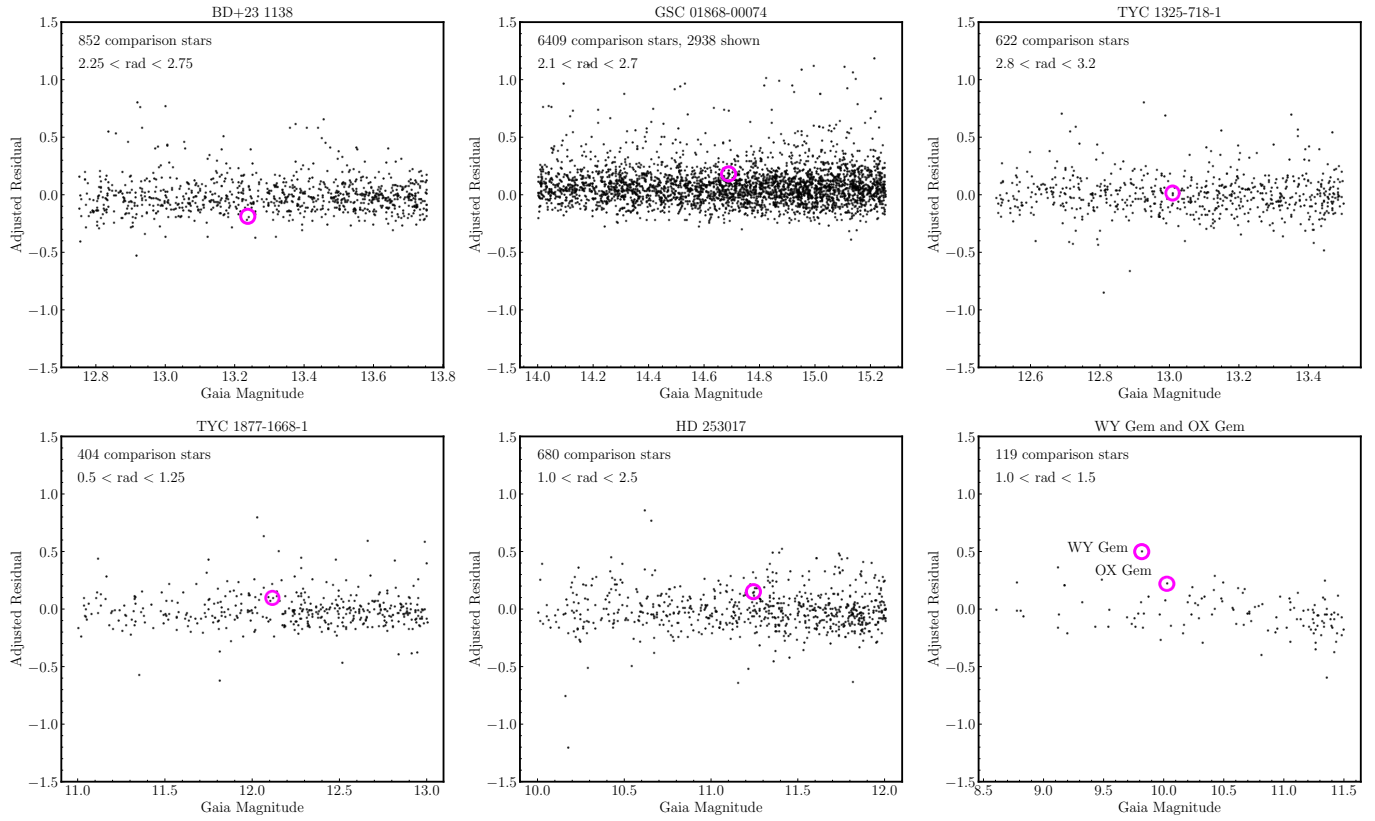
Figure 13. Stars 1, 2, 3, 5, 7, and a combination of 4 and 8 respectively (see Table 3). The magenta circles identify the star in question. The y-axis is the residual after removing the trend with *pg* and adjusting the mean to be zero. Thus the y-value of the magenta circle is the offset indicated in Table 3

correct for astrometric errors caused by the operation of the scanner; and we have implemented a more sophisticated photographic transformation of the plate scans that has allowed us to linearize our photometric magnitude scale over a wide range. Despite the challenges imposed by the difference in telescope and stellar crowding between the two papers, these improvements allow our results to remain comparable to those from Paper I.

We illustrated the quality of our measurements by comparing a small sample of red supergiant stars within the field of 10B-161 to individualized samples of astrometrically and photometrically similar stars. Our intent was to detect variability across our 117-year timescale within the stellar population captured on the plate. Only one star in our sample, WY Gem, was clearly detected to be variable, but this is probably due to the sample of red supergiants being overall relatively bright and therefore relatively challenging for our methods.

This study demonstrates the scientific potential of photographic plates: once appropriately digitized, they can be used to extend the range of stellar data to over a century. This increase of time baseline is invaluable to the study of long-term variability as well as other areas of time-domain astronomy. Our cost-effective methods make the data on these plates much more readily available to researchers in the field. As research continues, we plan to refine the methods described in this paper to establish a broadly applicable, cost-effective, and efficient pipeline for the production of high-quality photometric data from large collections of photographic plates.

REFERENCES

Astropy Collaboration, Robitaille, T. P., Tollerud, E. J., et al. 2013, A&A, 558, A33

Barbieri, C., Blanco, C., Bucciarelli, B., et al. 2003, Experimental Astronomy, 15, 29–43

Barnard, E. E., Frost, E. B., & Calvert, M. R. 1927, A photographic atlas of selected regions of the Milky Way (Carnegie Institution of Washington). https://exhibit-archive.library.gatech.edu/barnard/filename

Brown, A. G. A., Vallenari, A., Prusti, T., et al. 2021, Astronomy Astrophysics, 650, C3. http://dx.doi.org/10.1051/0004-6361/202039657e

Castelaz, M. W. 2009, in Astronomical Society of the Pacific Conference Series, Vol. 410, Preserving Astronomy's Photographic Legacy: Current State and the Future of North American Astronomical Plates, ed. W. Osborn & L. Robbins, 70

Cerny, W., Chapman, A., Glusman, R., et al. 2021, Publications of the Astronomical Society of the Pacific, 133, doi:10.1088/1538-3873/abec20

Federal Agencies Digital Guidelines Initiative. 2016,
    Technical Guidelines for Digitizing Cultural Heritage
    Materials: Creation of Raster Image Files.
    https://www.digitizationguidelines.gov/guidelines/
    FADGI%20Federal%20%20Agencies%20Digital%
    20Guidelines%20Initiative-2016%20Final_rev1.pdf

Glusman, R., Escapa, I., & Kron, R. G. 2022, Astronomical
    data and derivations from historic photographic glass
    plate 10B-161 from Yerkes Observatory Glass Plate
    collection, Knowledge@UChicago,
    doi:10.6082/UCHICAGO.3550.
    https://knowledge.uchicago.edu/record/3550

Hambly, N. C., Irwin, M. J., & MacGillivray, H. T. 2001,
    MNRAS, 326, 1295

Hunter, J. D. 2007, Computing In Science & Engineering,
    9, 90

Innis, J. L., Heil, P., Thompson, K., & Coates, D. W. 2004,
    Publications of the Astronomical Society of Australia, 21,
    284–289

Johnson, J. A., & Winn, J. N. 2004, AJ, 127, 2344

Kiss, L. L., Szabó, G. M., & Bedding, T. R. 2006, MNRAS,
    372, 1721

Kolesnikova, D. M., Sat, L. A., Sokolovsky, K. V., Antipin,
    S. V., & Samus, N. N. 2008, AcA, 58, 279

Kroll, P., & Neugebauer, P. 1993, A&A, 273, 341

Laher, R. R., Gorjian, V., Rebull, L. M., et al. 2012, PASP,
    124, 737

LaserSoft Imaging. 2011. https:
    //www.silverfast.com/show/lasersoftimaging/en.html

Lasker, B. M., Lattanzi, M. G., McLean, B. J., et al. 2008,
    AJ, 136, 735

Laycock, S., Tang, S., Grindlay, J., et al. 2010, AJ, 140,
    1062

Mandel, H., Birkle, K., Demleitner, M., & Heidelberg, L.
    2007, Wolf-Palisa Survey, VO resource provided by the
    GAVO Data Center, , ,
    doi:10.21938/haTEMZmoaCTEK6XZvGU.fQ.
    http://dc.zah.uni-heidelberg.de/lswscans/res/positions/
    wpshow/info

Messineo, M., & Brown, A. G. A. 2019, AJ, 158, 20

Moffat, A. F. J. 1969, A&A, 3, 455

Pakuliak, L., Kazantseva, L., Virun, N., & Andruk, V.
    2011, Proceedings of the International Astronomical
    Union, 7, 389–391

Price-Whelan, A. M., Sipőcz, B. M., Günther, H. M., et al.
    2018, AJ, 156, 123

Russell, J. L., Lasker, B. M., McLean, B. J., Sturch, C. R.,
    & Jenkner, H. 1990, AJ, 99, 2059

Samus, N. N., Kazarovets, E. V., Durlevich, O. V., Kireeva,
    N. N., & Pastukhova, E. N. 2017, Astronomy Reports,
    61, 80

Schindelin, J., Arganda-Carreras, I., Frise, E., et al. 2012,
    Nature Methods, 9, 676.
    https://doi.org/10.1038/nmeth.2019

Schlegel, D. J., Finkbeiner, D. P., & Davis, M. 1998, ApJ,
    500, 525

Schneider, C. A., Rasband, W. S., & Eliceiri, K. W. 2012,
    Nature Methods, 9, 671–675

Sharpless, S. 1959, ApJS, 4, 257

Shelton, I. 2009, ASP Conference Series, 410

Simcoe, R. J. 2009, in Astronomical Society of the Pacific
    Conference Series, Vol. 410, Preserving Astronomy's
    Photographic Legacy: Current State and the Future of
    North American Astronomical Plates, ed. W. Osborn &
    L. Robbins, 111

Sokolovsky, K. V., Zubareva, A. M., Kolesnikova, D. M.,
    et al. 2017, Proceedings of the International
    Astronomical Union, 14, 340–343

Tang, S., Grindlay, J., Los, E., & Servillat, M. 2013, PASP,
    125, 857

Taylor, M. B. 2005, in Astronomical Society of the Pacific
    Conference Series, Vol. 347, Astronomical Data Analysis
    Software and Systems XIV, ed. P. Shopbell, M. Britton,
    & R. Ebert, 29

Tsvetkov, M., Stavrev, K., Tsvetkova, K., et al. 2015,
    Wide-Field Plate Database WFPDB, VO resource
    provided by the GAVO Data Center, , .
    https://dc.zah.uni-heidelberg.de/wfpdb/q/cone/info

Van Der Walt, S., Colbert, S. C., & Varoquaux, G. 2011,
    Computing in Science & Engineering, 13, 22

van Leeuwen, F., de Bruijne, J., Babusiaux, C., et al. 2021

Vicente, B., Abad, C., & Garzón, F. 2007, Astronomy amp;
    Astrophysics, 471, 1077–1089

Virtanen, P., Gommers, R., Oliphant, T. E., et al. 2020,
    Nature Methods, 17, 261